J. Meas. Sci. Instrum., 2026, 17(1): 61-71.
DOI: 10.62756/jmsi.1674-8042.2026005
http://jmsi.publish.founderss.cn/
jmsi@nuc.edu.cn

Improved strong tracking Kalman filter algorithm based SINS/GNSS/ODO integrated navigation

CHUN Yi[1,2], CHEN Guangwu[2,3*], SI Yongbo[2,3], ZHOU Xin[2,3], YAN Yuqian[2,3]

1. School of Electronics and Information Engineering, Lanzhou Jiaotong University, Lanzhou 730070, China;
2. Gansu Provincial Key Laboratory of Traffic Information Engineering and Control, Lanzhou 730070, China;
3. School of Automation and Electrical Engineering, Lanzhou Jiaotong University, Lanzhou 730070, China

***Corresponding author:** CHEN Guangwu (cgwyjh101@126.com)

Received: December 5, 2024 **Revised:** February 22, 2025 **Accepted:** February 25, 2025

Abstract: The combination of strapdown inertial navigation system (SINS), global navigation satellite system (GNSS), and odometer (ODO) is the most practical and cost-effective way to implement a multi-source fusion automotive navigation system. However, the traditional Kalman filtering (KF) algorithm suffers from the inaccuracy of the system state matrix and the measurement noise covariance matrix during vehicle operation, which leads to a decrease in navigation and positioning accuracy. To solve this problem, a measurement adaptive strong tracking Kalman filter (MA-STKF) algorithm is proposed. The algorithm adopts an asymptotic weighting approach to estimate the measurement covariance array by considering new interest time series being actually filtered, introduces a measurement forgetting factor, perform real-time estimation and correction combines with the decay factor of the strong tracking filter, and takes advantage of the difference between the actual measurement error and the predicted covariance to reset the decay factor, which improves the tracking performance of the algorithm. The proposed algorithm is applied to the SINS/GNSS/ODO integrated navigation system, and simulation and vehicle experiments were conducted, improving the positioning longitude by 52.48% and 30.96%, and the positioning latitude by 63.27% and 37.64%, compared to KF and STKF, respectively.

Key words: Kalman filtering (KF); integrated navigation; strong tracking filter (STF); measurement adaptation; forgetting factor

0 Introduction

Strapdown inertial navigation system (SINS) and global navigation satellite system (GNSS) exhibit a high degree of complementarity, enabling them to consistently and stably output smooth, high-sampling-rate positioning results in complex environments, and have been widely used in vehicle integrated navigation systems[1-4]. Nevertheless, in the context of GNSS denial, the cumulative error of SINS is challenging to eradicate due to the interference of satellite signals, which results in a precipitous decline in positioning accuracy at this time. Consequently, supplementary data must be incorporated to rectify the cumulative error of SINS[5-6]. The odometer (ODO) is a passive and autonomous onboard sensor that is frequently employed in conjunction with an SINS/GNSS integrated navigation system. By outputting incremental positional data and utilizing dead reckoning (DR), it enables fully autonomous navigation and effectively suppresses the error divergence of the inertial guidance system during prolonged periods of GNSS signal denial[7-8].

Kalman filtering (KF) is a widely utilized filtering algorithm for navigation. However, the process noise and measurement noise of the KF are often unknown or time-varying while the vehicle is travelling. A sudden alteration in the carrier state may produce a deterioration of the state estimation accuracy, potentially leading to filter divergence in severe cases[9-11], and resulting in a decrease in vehicle positioning accuracy. In order to address the aforementioned issues, a multitude of scholars have conducted research and proposed a number of potential solutions. These include the Kalman filter with forgetting factor (KFFF) [12-13], the Sage-Husa adaptive Kalman filter (SHAKF) [14-15], and the chi-square test adaptive Kalman filter (CSTAKF) [16]. The forgetting factor filter algorithm modifies both the system noise and the measurement noise in the filtering process through the introduction of a forgetting factor. This results in a gradual reduction of the weight

attributed to historical information, thereby reducing the inertia of the filter. However, it should be noted that this approach does not allow for the achievement of optimal estimation, and the enhancement of the vehicle positioning accuracy is limited. The Sage-Husa adaptive filter is capable of dynamically estimating and adjusting the covariance matrices of the process noise and measurement noise, thereby enabling the filter to adapt to changes in the system state and measurement noise. Nevertheless, the efficacy of this filter is contingent upon the initial conditions, and inappropriate initial selections can significantly impair the accuracy of the filtering process. The soft chi-square test adaptive filtering method employs a selected threshold to determine the gate limit for the isolation of anomalous measurements, and the filtering gain is adjusted dynamically through the application of the soft chi-square test of residuals, thereby enhancing the overall filtering performance. Nevertheless, the method requires the setting of a reasonable threshold and other parameters, which may be challenging to determine them and difficult to use them in complex environments.

In response to this, Zhou et al.[17] put forth a robust tracking filter based on the tenet of innovation orthogonality. In comparison to alternative filters, the strong tracking filter exhibits enhanced tracking capabilities in the event of alterations to the model parameters or abrupt changes in the system. Additionally, it demonstrates reduced sensitivity to the statistical attributes of noise and initial values. In this study, Hu et al.[18-19] examined the efficacy of the strong tracking Kalman filter (STKF) in addressing the shortcomings of traditional Kalman filtering in highly dynamic and nonlinear scenarios. They introduced residual adaptive adjustment and a robust tracking mechanism to enhance the filter's performance in such complex environments and improve vehicle navigation and positioning accuracy. Based on this foundation, Li et al. [20-21] used multiple fading factors to adjust the predicted state covariance matrix, ensuring that different filtering channels have different fading capabilities, thus achieving strong tracking of the vehicle's true state. However, the STKF algorithm is more complex to configure the settings in complex multivariate systems, and there is a difficulty in needing different adjustments for different filtering channels. In order to address the impact of measurement noise caused by environmental changes, we propose a novel measurement adaptive strong tracking Kalman filter (MA-STKF) method. Based on the STKF algorithm, it obtains the innovation variance matrix through an asymptotic weighting method, designs measurement fault detection and isolation to reduce the adverse effects of harmful measurements, and introduces a forgetting factor to adjust the measurement noise variance so as to overcome the divergence issues present in STKF. The improved algorithm takes into account the real-time requirements of navigation and positioning in real-world applications, and uses a simple and effective method to optimize the algorithm, reduce arithmetic complexity, and provide reliable positioning information. The proposed algorithm was implemented in a SINS/GNSS/ODO integrated navigation system for the purposes of simulation and vehicle experiment validation. The findings demonstrate that when the system is subjected to inaccurate noise processing and measurement, the MA-STKF algorithm exhibits a substantial superiority over the KF and STKF algorithms, notably enhancing the filtering precision of the integrated navigation system.

1 Measurement adaptive strong tracking Kalman filter (MA-STKF)

1.1 Strong tracking filter

The strong tracking filter (STF) exhibits exemplary tracking capabilities and is capable of responding effectively to abrupt alterations in system states. It is capable of overcoming issues where the filter is unable to accurately track system states or becomes ineffective due to uncertainties in the system model. Let us consider a class of discrete nonlinear systems, as illustrated in

$$\boldsymbol{x}_{k+1}=f(\boldsymbol{x}_k,\boldsymbol{u}_k)+\boldsymbol{\Gamma}_k\boldsymbol{w}_k, \tag{1}$$

$$\boldsymbol{z}_{k+1}=h(\boldsymbol{x}_{k+1})+\boldsymbol{v}_{k+1}, \tag{2}$$

where the discrete time variable k, the state vector of the system $\boldsymbol{x}_k$, the observation vector of the system $\boldsymbol{z}_k$, the input vector $\boldsymbol{u}_k$, the noise-driven array $\boldsymbol{\Gamma}_k$, the process noise of the system $\boldsymbol{w}_k$, the measurement noise of the system $\boldsymbol{v}_k$, and the statistical properties, as shown in Eqs. (3) — (5), are all of significance.

$$E(\boldsymbol{w}_k)=0,\ Cov(\boldsymbol{w}_k,\boldsymbol{w}_j)=\boldsymbol{Q}_k\boldsymbol{\delta}_{kj}, \tag{3}$$

$$E(\boldsymbol{v}_k)=0,\ Cov(\boldsymbol{v}_k,\boldsymbol{v}_j)=\boldsymbol{R}_k\boldsymbol{\delta}_{kj}, \tag{4}$$

$$Cov(\boldsymbol{w}_k,\boldsymbol{v}_j)=0, \tag{5}$$

where $\boldsymbol{Q}_k$ represents a symmetric non-negative definite matrix, whereas $\boldsymbol{R}_k$ denotes a symmetric positive definite matrix. The STF is responsible for ensuring that the residual sequence of the filtered output is Gaussian white noise. This is achieved by adjusting the filter gain

matrix online in real time, as illustrated in

$$E\left[\left(\boldsymbol{x}_{k+1}-\bar{\boldsymbol{x}}_{k+1}\right)\left(\boldsymbol{x}_{k+1}-\bar{\boldsymbol{x}}_{k+1}\right)^{\mathrm{T}}\right]=\min, \tag{6}$$

$$\boldsymbol{V}_{j,k+1}=\boldsymbol{E}\left[\boldsymbol{\gamma}_{k+1}\boldsymbol{\gamma}_{k+1+j}^{\mathrm{T}}\right]=0. \tag{7}$$

Eqs. (6) and (7) allow the robust tracking filter to satisfy the minimum variance estimation performance index, while ensuring that the residual sequences of the filter remain orthogonal. This design can fully extract the effective information present in the residual sequences, thereby effectively overcoming the filter performance degradation that may occur in the presence of model uncertainty or sudden state changes. Consequently, the robust tracking filter is highly adaptive to model uncertainty and exhibits a remarkable ability to track abrupt state transitions.

1.2 Measurement adaptive Kalman filter

Theoretically, the innovation sequence of the standard Kalman filter is white noise[22]. By rewriting the innovation expression and organizing it according to the geometric interpretation of KF and the properties of orthogonal projections, the following result is obtained as[23]

$$\begin{gathered}\boldsymbol{Z}_{k/k-1}=\boldsymbol{Z}_k-\boldsymbol{H}_k\hat{\boldsymbol{X}}_{k/k-1}=\\ \boldsymbol{Z}_k-\boldsymbol{H}_k\boldsymbol{\Phi}_{k/k-1}\hat{\boldsymbol{X}}_{k-1}=\\ \boldsymbol{H}_k\left(\boldsymbol{\Phi}_{k/k-1}\boldsymbol{X}_{k-1}+\boldsymbol{\Gamma}_{k-1}\boldsymbol{W}_{k-1}\right)+\\ \boldsymbol{V}_k-\boldsymbol{H}_k\boldsymbol{\Phi}_{k/k-1}\hat{\boldsymbol{X}}_{k-1}=\\ \boldsymbol{H}_k\boldsymbol{\Phi}_{k/k-1}\left(\boldsymbol{X}_{k-1}-\hat{\boldsymbol{X}}_{k-1}\right)+\\ \boldsymbol{H}_k\boldsymbol{\Gamma}_{k-1}\boldsymbol{W}_{k-1}+\boldsymbol{V}_k=\\ \boldsymbol{H}_k\boldsymbol{\Phi}_{k/k-1}\boldsymbol{X}_{k-1}+\boldsymbol{H}_k\boldsymbol{\Gamma}_{k-1}\boldsymbol{W}_{k-1}+\boldsymbol{V}_k,\end{gathered} \tag{8}$$

where $\boldsymbol{Z}_k$ is the observation at the current moment k, $\boldsymbol{H}_k$ is the observation matrix, $\hat{\boldsymbol{X}}_{k/k-1}$ is the predicted system state, $\boldsymbol{\Phi}_{k/k-1}$ the state transfer matrix, $\boldsymbol{\Gamma}_{k-1}$ is the control input, $\boldsymbol{W}_{k-1}$ is the observation noise, and $\boldsymbol{V}_k$ denotes the difference between the actual and predicted observations. It is evident that, given the unbiased nature of state estimation, the equation $E\left[\tilde{\boldsymbol{Z}}_{k/k-1}\right]=0$ is applicable. When $\tilde{\boldsymbol{Z}}$ and $\boldsymbol{Z}^{\mathrm{T}}$ are concurrent, the correlation between $\boldsymbol{X}_{k-1}$, $\boldsymbol{W}_{k-1}$, and $\boldsymbol{V}_k$ is complementary, and the three are evident in the time series, which allows us to conclude that

$$\begin{gathered}E\left[\tilde{\boldsymbol{Z}}_{k/k-1}\boldsymbol{Z}_{k/k-1}^{\mathrm{T}}\right]=\boldsymbol{H}_k\boldsymbol{\Phi}_{k/k-1}\boldsymbol{P}_{k-1}\boldsymbol{\Phi}_{k/k-1}^{\mathrm{T}}\boldsymbol{H}_k^{\mathrm{T}}+\\ \boldsymbol{H}_k\boldsymbol{\Gamma}_{k-1}\boldsymbol{Q}_{k-1}\boldsymbol{\Gamma}_{k-1}^{\mathrm{T}}\boldsymbol{H}_k^{\mathrm{T}}+\boldsymbol{R}_k.\end{gathered} \tag{9}$$

In this instance, an asymptotic weighting method is utilized for the estimation of the covariance matrix, derived from the actual filtered innovation time series, in accordance with the following procedure as[24]

$$\hat{\boldsymbol{C}}_k=\left(1-\beta_k\right)\hat{\boldsymbol{C}}_{k-1}+\beta_k\tilde{\boldsymbol{Z}}_{k/k-1}\tilde{\boldsymbol{Z}}_{k/k-1}^{\mathrm{T}}. \tag{10}$$

The estimate of the covariance of the new interest series represented by $\hat{\boldsymbol{C}}_k$ describes the quantification of the uncertainty about the state of the system. Among them,

$$\beta_k=\frac{\beta_{k-1}}{\beta_{k-1}+b}, \tag{11}$$

where the initial value $\beta_k=1$, and $0<b<1$ is called the asymptotic cancellation factor. The smaller the fade factor b, the more adaptable to new measurements of noise changes. b is often taken as 0.95—0.99. It should be noted that the fade factor b cannot be too small, otherwise the noise estimation results will jump too drastically. After repeated verification, we set $b=0.987$[25]. In the event that the residual sequence is consistent with a Gaussian white noise distribution, the theoretical expected value of the new interest covariance array is observed to be in close alignment with the actual estimated value. Consequently, Eq. (9) can be approximated as Eq. (10), that is to say,

$$\begin{gathered}\hat{\boldsymbol{C}}_k\approx\\ \boldsymbol{H}_k\left(\boldsymbol{\Phi}_{k/k-1}\boldsymbol{P}_{k-1}\boldsymbol{\Phi}_{k/k-1}^{\mathrm{T}}+\boldsymbol{\Gamma}_{k-1}\boldsymbol{Q}_{k-1}\boldsymbol{\Gamma}_{k-1}^{\mathrm{T}}\right)\boldsymbol{H}_k^{\mathrm{T}}+\boldsymbol{R}_k.\end{gathered} \tag{12}$$

The estimation of the new interest covariance array may be affected by factors that deviate from the norm, such as sudden changes in noise or state. These factors may lead to abnormal fluctuations in the filter, resulting in a significant mismatch between the calculated and theoretical expectations for the new interest. Consequently, the calculated new interest covariance array, as described in Eq.(10), may deviate from the expected theoretical outcome. In order to mitigate the adverse effects of erroneous measurements, an anomaly detection judgement is undertaken, where all measurements are considered collectively. In accordance with the stipulations set forth in Eq.(13), the filtering process is terminated and measurement updates are no longer conducted.

$$\begin{gathered}tr(\hat{\boldsymbol{C}}_k)\gg tr(\boldsymbol{H}_k(\boldsymbol{\Phi}_{k/k-1}\boldsymbol{P}_{k-1}\boldsymbol{\Phi}_{k/k-1}^{\mathrm{T}}+\\ \boldsymbol{\Gamma}_{k-1}\boldsymbol{Q}_{k-1}\boldsymbol{\Gamma}_{k-1}^{\mathrm{T}})\boldsymbol{H}_k^{\mathrm{T}}+\boldsymbol{R}_k).\end{gathered} \tag{13}$$

In instances where new interest mismatch symptoms are relatively mild, it is determined that the measurement variance array is subject to bias. Consequently, Eq. (12) is derived by shifting the terms as

$$\begin{gathered}\hat{\boldsymbol{C}}_k-\boldsymbol{H}_k(\boldsymbol{\Phi}_{k/k-1}\boldsymbol{P}_{k-1}\boldsymbol{\Phi}_{k/k-1}^{\mathrm{T}}+\\ \boldsymbol{\Gamma}_{k-1}\boldsymbol{Q}_{k-1}\boldsymbol{\Gamma}_{k-1}^{\mathrm{T}})\boldsymbol{H}_k^{\mathrm{T}}=\boldsymbol{R}_k.\end{gathered} \tag{14}$$

Subsequently, a comprehensive alteration of its dimensions is conducted in real time through the incorporation of a forgetting factor, as illustrated in Eq. (14). This results in the following adjustment as

$$\hat{C}_k - H_k(\boldsymbol{\Phi}_{k/k-1}P_{k-1}\boldsymbol{\Phi}_{k/k-1}^{\mathrm{T}} + \boldsymbol{\Gamma}_{k-1}\boldsymbol{Q}_{k-1}\boldsymbol{\Gamma}_{k-1}^{\mathrm{T}})H_k^{\mathrm{T}} = \alpha_k \boldsymbol{R}_k. \tag{15}$$

The forgetting factor is defined as

$$\alpha_k = \frac{tr\left(\hat{C}_k - H_k\left(\boldsymbol{\Phi}_{k/k-1}P_{k-1}\boldsymbol{\Phi}_{k/k-1}^{\mathrm{T}} + \boldsymbol{\Gamma}_{k-1}\boldsymbol{Q}_{k-1}\boldsymbol{\Gamma}_{k-1}^{\mathrm{T}}\right)H_k^{\mathrm{T}}\right)}{tr(\boldsymbol{R}_k)}. \tag{16}$$

The adaptation of the measurement noise variance is achieved by replacing $\boldsymbol{R}_k$ with the corrected $\alpha_k \boldsymbol{R}_k$ for the Kalman filter measurement update.

1.3 MA-STKF

Should the system parameters $\boldsymbol{\Phi}_{k/k-1}$, $\boldsymbol{\Gamma}_{k-1}$, H_k, $\boldsymbol{Q}_k$ or $\boldsymbol{R}_k$ undergo alteration during the filtering process, the accuracy of the state estimation will decline in direct correlation with the progression of the filtering. Accordingly, Eq. (15) is modified as

$$\hat{C}_k - H_k\boldsymbol{\Gamma}_{k-1}\boldsymbol{Q}_{k-1}\boldsymbol{\Gamma}_{k-1}^{\mathrm{T}}H_k^{\mathrm{T}} - \boldsymbol{R}_k = H_k\boldsymbol{\Phi}_{k/k-1}P_{k-1}\boldsymbol{\Phi}_{k/k-1}^{\mathrm{T}}H_k^{\mathrm{T}} = C_i. \tag{17}$$

The incorporation of a suboptimal fading factor λ_k into Eq. (17) for the real-time adjustment of the one-step predicted error covariance matrix $P_{k/k-1}$ and the corresponding estimator gain matrix $\boldsymbol{K}_k$ of the augmented state has the potential to markedly enhance the tracking capability of the estimator for changing states. The incorporation of this adjustment mechanism enables the filter to retain its capacity for high adaptability and accuracy in the context of evolving states. Accordingly, Eq. (16) is modified as

$$\hat{C}_k - H_k\boldsymbol{\Gamma}_{k-1}\boldsymbol{Q}_{k-1}\boldsymbol{\Gamma}_{k-1}^{\mathrm{T}}H_k^{\mathrm{T}} - \boldsymbol{R}_k = H_k\boldsymbol{\Phi}_{k/k-1}(\lambda_k P_{k-1})\boldsymbol{\Phi}_{k/k-1}^{\mathrm{T}}H_k^{\mathrm{T}}. \tag{18}$$

In this approach, both sides are employed concurrently for the matrix trace operation, with the understanding that the scale factor a must be greater than or equal to 1. This yields the following result as

$$\lambda_k = \max\left(1, \frac{tr(\boldsymbol{N}_k)}{tr(\boldsymbol{M}_k)}\right), \tag{19}$$

where

$$\boldsymbol{N}_k = \hat{C}_k - H_k\boldsymbol{\Gamma}_{k-1}\boldsymbol{Q}_{k-1}\boldsymbol{\Gamma}_{k-1}^{\mathrm{T}}H_k^{\mathrm{T}} - \boldsymbol{R}_k. \tag{20}$$

$$\boldsymbol{M}_k = H_k\boldsymbol{\Phi}_{k/k-1}P_{k-1}\boldsymbol{\Phi}_{k/k-1}^{\mathrm{T}}H_k^{\mathrm{T}}. \tag{21}$$

At this juncture, the equation for measurement-adaptive tracking Kalman filtering is

$$\hat{\boldsymbol{X}}_{k/k-1} = \boldsymbol{\Phi}_{k/k-1}\hat{\boldsymbol{X}}_{k-1}. \tag{22}$$

$$P_{k/k-1} = \boldsymbol{\Phi}_{k/k-1}(\lambda_k P_{k-1})\boldsymbol{\Phi}_{k/k-1}^{\mathrm{T}} + \boldsymbol{\Gamma}_{k-1}\boldsymbol{Q}_{k-1}\boldsymbol{\Gamma}_{k-1}^{\mathrm{T}}. \tag{23}$$

$$\boldsymbol{K}_k = P_{k/k-1}H_k^{\mathrm{T}}\left(H_k P_{k/k-1}H_k^{\mathrm{T}} + \alpha_k \boldsymbol{R}_k\right)^{-1}. \tag{24}$$

$$\hat{\boldsymbol{X}}_k = \hat{\boldsymbol{X}}_{k/k-1} + \boldsymbol{K}_k\left(\boldsymbol{Z}_k - H_k\hat{\boldsymbol{X}}_{k/k-1}\right). \tag{25}$$

$$P_k = (\boldsymbol{I} - \boldsymbol{K}_k H_k)P_{k/k-1}. \tag{26}$$

The flowchart of the measurement adaptive strong tracking Kalman filtering algorithm is presented in Fig. 1.

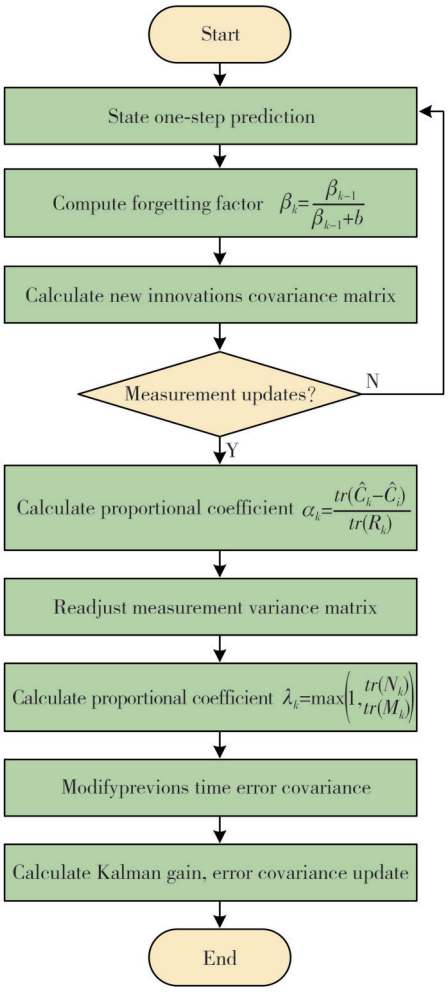

Fig. 1 Flowchart of measurement adaptive strong tracking Kalman filter algorithm

2 SINS/GNSS/ODO integrated navigation system model

In order to verify the efficacy of the algorithm presented in this paper, an SINS/GNSS/ODO integrated navigation system model is selected, employing a loose combination strategy. The "East-North-Up (E-N-U)" geographic coordinate system is utilized as the navigation reference coordinate system for the strapdown inertial navigation system. The 18-dimensional system state vector is defined as

$$\boldsymbol{X} = \left[\boldsymbol{\Phi}^{\mathrm{T}} \ \left(\boldsymbol{\delta}_{v^n}\right)^{\mathrm{T}} \ (\boldsymbol{\delta}_{\mathrm{p}})^{\mathrm{T}} \ (\boldsymbol{\delta}_{p_{\mathrm{U}}})^{\mathrm{T}} \ \left(\boldsymbol{\varepsilon}^b\right)^{\mathrm{T}} \ \left(\nabla^b\right)^{\mathrm{T}}\right]^{\mathrm{T}}, \tag{27}$$

where $\boldsymbol{v}$ represents the white noise of the position measurement of the guide receiver. The variables $\boldsymbol{\Phi}^{\mathrm{T}} = (\phi_{\mathrm{E}}, \phi_{\mathrm{N}}, \phi_{\mathrm{U}})^{\mathrm{T}}$, $(\boldsymbol{\delta}_{v^n})^{\mathrm{T}} = (\delta_{v_{\mathrm{E}}}, \delta_{v_{\mathrm{N}}}, \delta_{v_{\mathrm{U}}})^{\mathrm{T}}$, $(\boldsymbol{\delta}_{\mathrm{P}})^{\mathrm{T}} = (\delta_{p_{\mathrm{E}}}, \delta_{p_{\mathrm{N}}},$

$\delta_{p_U})^T$, $(\boldsymbol{\delta}_{P_D})^T=(\delta_{p_{D_E}},\delta_{p_{D_N}},\delta_{p_{D_U}})^T$, $\boldsymbol{\varepsilon}^b$, and ∇^b correspond to the platform misalignment angle, velocity error, position error, odometer position error, gyro random constant drift, and accelerometer random constant bias, respectively. In the course of the vehicle experiments, a conventional odometer calibration method was employed, whereby the odometer was calibrated based on the distance travelled by the vehicle and the total number of pulses output by the odometer. Following calibration, the odometer scale factor coefficient was determined to be 0.189 8.

In the context of integrated navigation, the position information and velocity differences output by SINS and GNSS, along with misalignment angle errors, are employed as measurements. Furthermore, the influence of satellite lever arm inaccuracies $\delta\boldsymbol{l}^b$ on velocity and position within the vehicle coordinate system must be taken into account.

$$\boldsymbol{Z}_{\mathrm{SINS/GNSS}}=\begin{bmatrix}\boldsymbol{\Phi}\\ \boldsymbol{V}_{\mathrm{SINS}}-\boldsymbol{V}_{\mathrm{GNSS}}+\delta\boldsymbol{V}_l\\ \boldsymbol{P}_{\mathrm{SINS}}-\boldsymbol{P}_{\mathrm{GNSS}}+\delta\boldsymbol{P}_l\end{bmatrix}. \tag{28}$$

$$\boldsymbol{H}_{\mathrm{SINS/GNSS}}=[\boldsymbol{I}_{9\times 9}\quad \boldsymbol{O}_{9\times 9}]. \tag{29}$$

In the case of SINS/ODO integrated navigation, the discrepancy between the position data obtained from the inertial navigation system and that derived from the odometer is employed as the basis for measurement.

$$\boldsymbol{Z}_{\mathrm{SINS/ODO}}=[\boldsymbol{P}_{\mathrm{SINS}}-\boldsymbol{P}_{\mathrm{ODO}}]. \tag{30}$$

$$\boldsymbol{H}_{\mathrm{SINS/ODO}}=[\boldsymbol{O}_{3\times 15}\quad \boldsymbol{I}_{3\times 3}]. \tag{31}$$

The observation errors are processed through filters and fed back into the SINS, where they are compensated and corrected. This results in enhanced navigation accuracy and stability for the SINS.

Fig.2 presents a block diagram of the integrated SINS/GNSS/ODO-based navigation system.

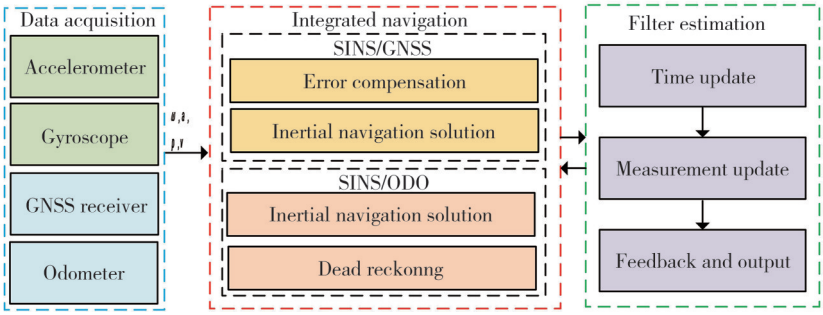

Fig. 2 Block diagram of SINS/GNSS/ODO integrated navigation

3 Experiment and analysis

3.1 Simulation

The effectiveness of the proposed method was verified on Matlab and the relevant simulation parameters are set as follows.

The right front upper lever arm error in Table 1 is used to compensate for the error between the satellite and the inertial measurement unit; the gyroscope and accelerometer zero bias and angular random wander are inherent errors of the devices, and the parameters are set with reference to MEMS inertial measurement unit STIM300. To simulate the effects of complex environments, the simulation trajectory is configured with multi-motion scenarios, including stationary, acceleration, deceleration, and cornering. Additionally, the satellite loss of lock is set up with varying timeframes, from 100 s to 300 s and from 550 s to 650 s. The real motion trajectories of KF, STF and MA-STKF are illustrated in Fig.3.

As illustrated in Fig. 3, the trajectories of the three methods exhibit a high degree of alignment with the reference trajectory. The trajectory of MA-STKF is in closer alignment with the reference trajectory, indicating higher positioning accuracy.

Table 1 Simulation parameter settings

Parameter	Value
Initial latitude/(°)	36
Initial longitude/(°)	100
Initial direction angle/(°)	90
Initial pitch angle/(°)	0
Initial roll angle/(°)	0
Latitude/longitude error/(°)	$1.567\,85\times 10^{-7}$
Horizontal attitude angle error/(°)	1
Initial heading error/(°)	1
Initial horizontal speed error/(m•s^{-1})	0.03
Right front upper lever arm error/m	0.05, 1.33, 1.05
Odometer scale error/%	0.05
Gyro zero-bias stability/((°)•h^{-1})	8
Gyroscope angle wanders randomly/((°)•h$^{-\frac{1}{2}}$)	0.2
Acceleration zero-bias instability/mg	0.05
Accelerometer speeds travelling randomly/(μg•h$^{-\frac{1}{2}}$)	700

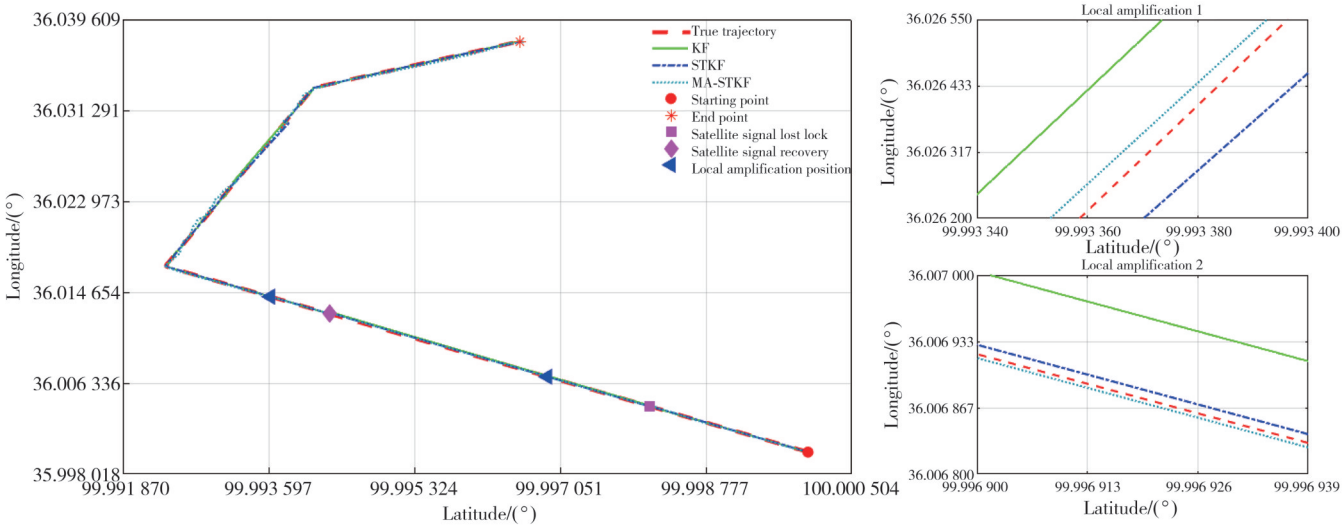

Fig. 3 Simulated motion trajectory

Figs.4—6 show the comparison of longitude, latitude and altitude errors of the three methods. Figs.7—8 show the comparison of eastward and northward speed errors. Figs.9—11 show the comparison of heading angle, pitch angle, and roll angle errors.

Table 2 shows the root mean square errors (RMSEs) and mean absolute deviations (MADs) of the latitude, longitude, eastward speed, and northward speed of the three methods.

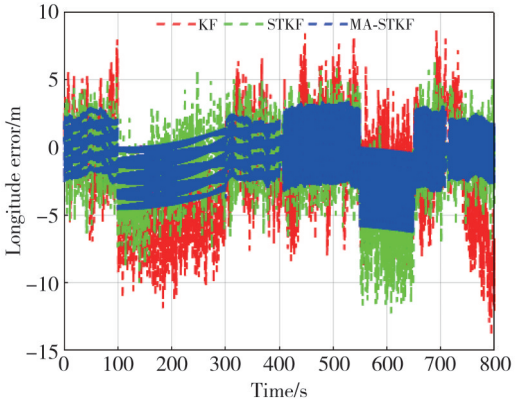

Fig. 4 Simulated longitude errors

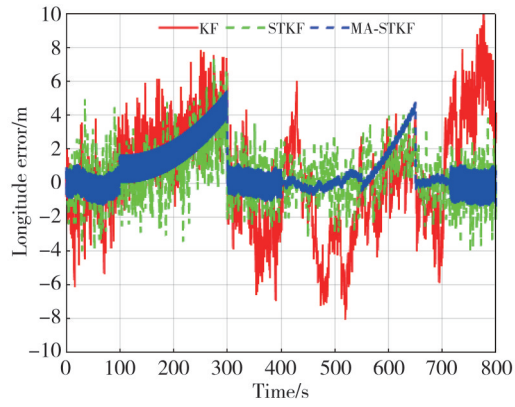

Fig. 5 Simulated latitude errors

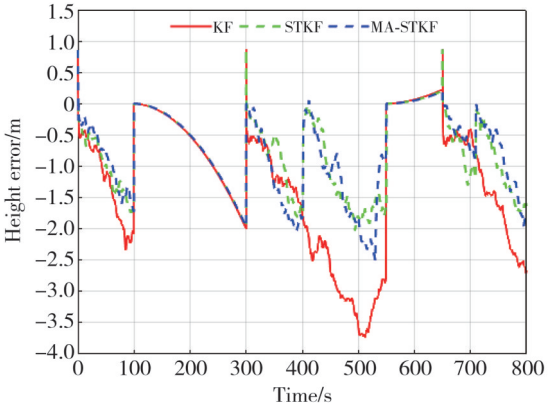

Fig. 6 Simulated height errors

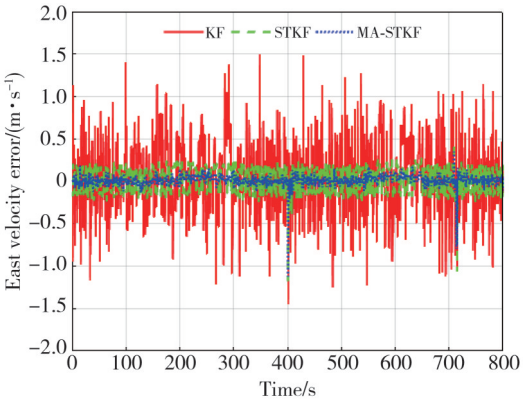

Fig. 7 Simulated eastward speed errors

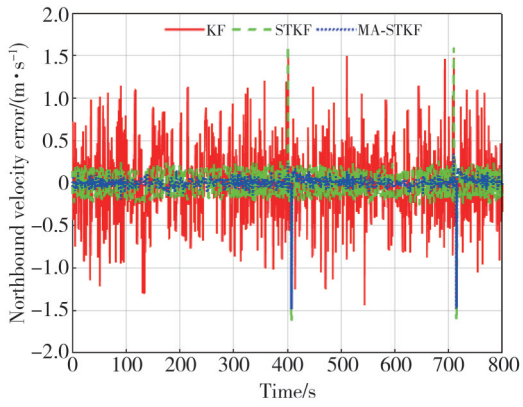

Fig. 8 Simulated northward speed errors

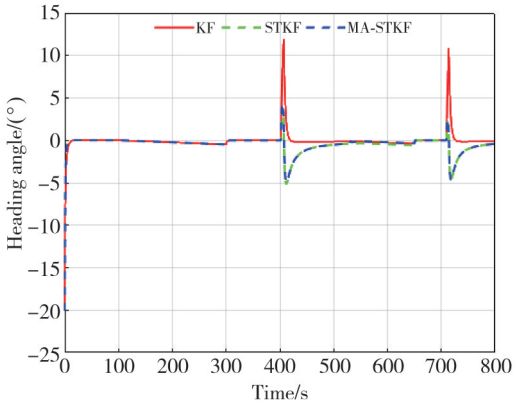

Fig. 9 Comparison of heading angle errors

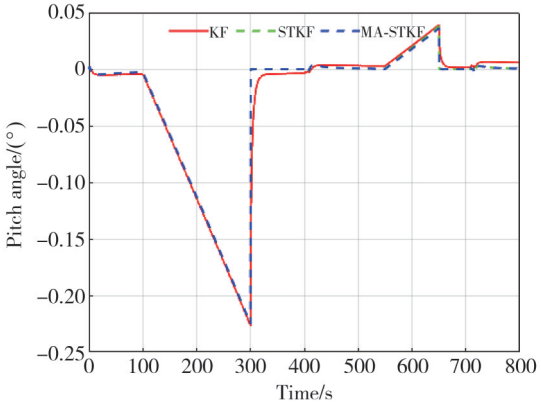

Fig. 10 Comparison of pitch angle errors

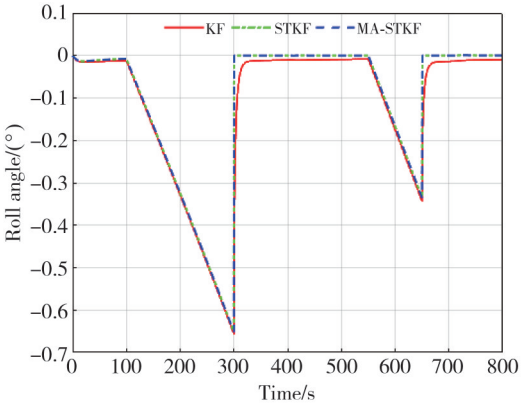

Fig. 11 Comparison of roll angle errors

As illustrated in Table 2, the RMSEs and the MADs of the longitude, latitude, eastward speed and northward speed of MA-STKF are observed to be smaller than those of KF and STF. Furthemore, the results of RMSE demonstrate that the MA-STKF produces estimates that are in close proximity to the true values for the majority of the datasets. Additionally, the MAD results indicate that the MA-STKF has robust performance and is capable of effectively mitigating the impact of anomalous errors, accordingly offering not only more precise estimation but also robust stability and noise immunity.

Table 2 Comparison of RMSEs and MADs in simulation

Algorithm	RMSE				MAD			
	Longitude/m	Latitude/m	Eastward speed/($m \cdot s^{-1}$)	Northward speed/($m \cdot s^{-1}$)	Longitude/m	Latitude/m	Eastward speed/($m \cdot s^{-1}$)	Northward speed/($m \cdot s^{-1}$)
KF	4.257 6	3.251 6	0.223 2	0.208 1	3.473 8	2.651 1	0.329 2	0.313 0
STKF	3.194 3	1.530 9	0.149 6	0.151 9	2.390 7	1.161 7	0.153 9	0.164 5
MA-STKF	**2.070 0**	**1.488 1**	**0.029 0**	**0.030 8**	**1.650 4**	**0.973 7**	**0.045 9**	**0.063 3**

Table 3 shows the simulated MADs of latitude, longitude, eastward speed, and northward speed. It can be seen that the MADs in longitude and latitude using MA-STKF are superior to those using KF and STKF. The STKF and MA-STKF demonstrate superior performance compared to the traditional KF, with improvements of 52% and 30% in the positioning longitude and of 63% and 37% in the positioning latitude, respectively. The speed errors in the east direction have the improvements of 86% and 77% and in the north direction have the improvements of 85% and 68%, respectively..

Table 3 Comparison of MADs in simulation

Algorithm	MAD			
	Longitude/m	Latitude/m	Eastward speed/($m \cdot s^{-1}$)	Northward speed/($m \cdot s^{-1}$)
KF	3.473 8	2.651 1	0.223 2	0.208 0
STKF	2.390 6	1.561 6	0.131 0	0.097 2
MA-STKF	**1.650 4**	**0.973 7**	**0.029 0**	**0.030 8**

3.2 Vehicle experiment

To further validate the effectiveness of the proposed method, vehicle experiment was conducted. The experiment was conducted in the vicinity of Jian'an East Road, Anning District, Lanzhou City, Gansu Province. The experimental apparatus included intertial measurement unit (IMU), GNSS receivers, inertial navigation systems, mobile power supplies, and other pertinent equipment. Inertial navigation systems were installed within the carriages. The total length of the test track was 2 600 m with a total test time of 1 400 s. The satellite was manually set to lose lock between 385 s and 725 s for a period of 340 s while the vehicle was in motion. Table 4 presents the

specifications of the gyroscope and accelerometer sensors utilized in the experimental procedure.

Table 4 Sensor parameters

Parameter	Value
Zero bias stability/((°)•h^{-1})	5
Random angle wandering/((°)•h$^{-\frac{1}{2}}$)	0.15
Zero bias instability/mg	0.02
Speed randomised roaming/(μg•h$^{-\frac{1}{2}}$)	700
Update frequency/Hz	125

Fig. 12 illustrates the trajectories of the vehicle during the experiment. The motion trajectories of on-board experiments, KF, STKF, and MA-STKF are illustrated in Fig. 13. The dark red square represents the starting point of the loss of lock, while the dark red rhombus depicts the recovery point of the loss of lock.

As illustrated in Fig. 13, the trajectories of three methods exhibit a high degree of alignment with the original trajectories under the vehicle test.

Fig. 12 Vehicle track diagram

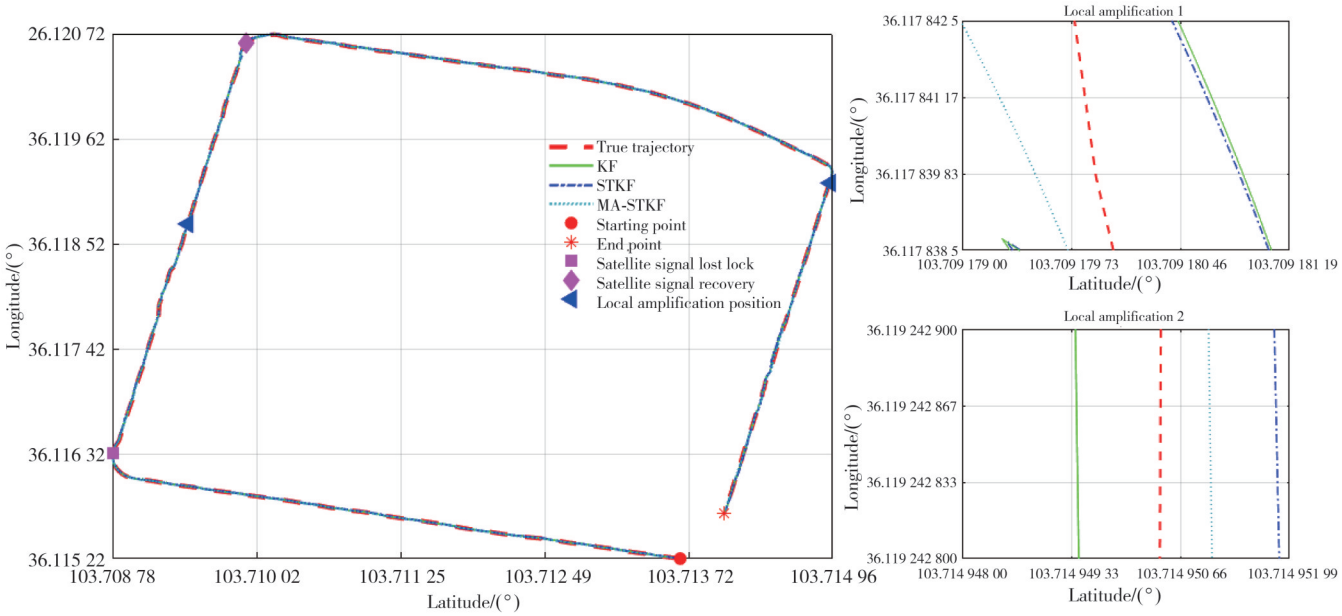

Fig. 13 Comparison chart of vehicle experimental trajectories

Figs. 14—15 present the comparison of the longitude and latitude errors for the three methods employed in the sports vehicle experiment. It can be observed that the latitude and longitude errors of the proposed MA-STKF method are stable within a certain range.

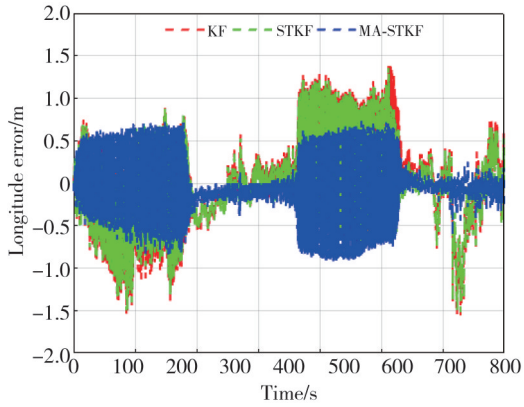

Fig. 14 Longitude error of vehicle-based experiment

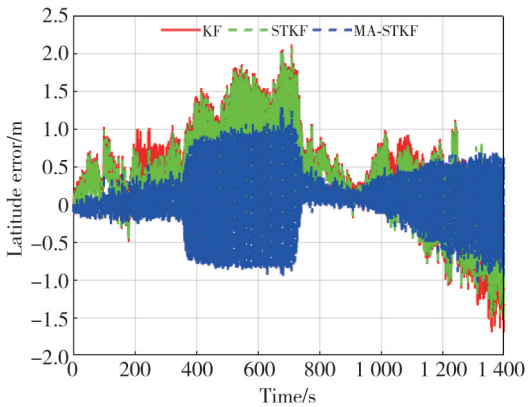

Fig. 15 Latitude error of vehicle-based experiment

In contrast, the traditional KF and SKF exhibit larger fluctuations. This suggests that the proposed method is capable of effectively addressing the inaccuracies in system states and measurements caused by changes in the external environment during actual road testing conditions.

Figs.16—17 present the comparison of the probability density values of the latitude and longitude errors associated with the three methods under investigation in the context of the sports vehicle experiment.

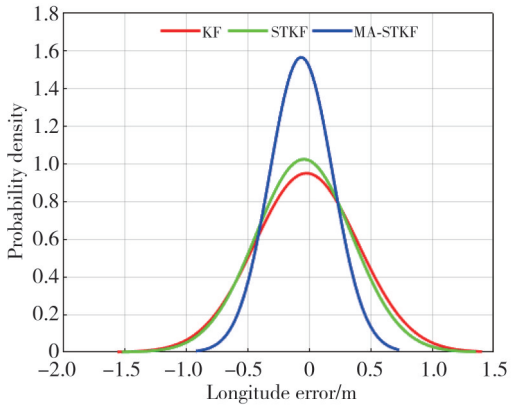

Fig. 16 Probability density of longitude error

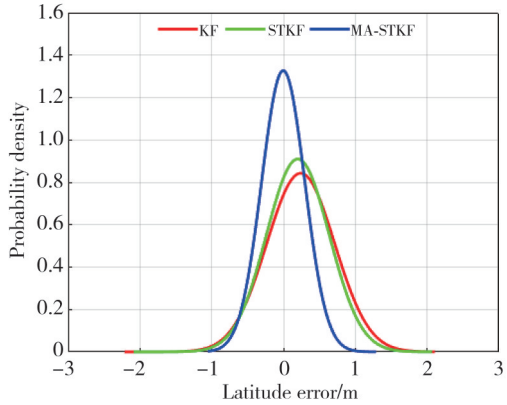

Fig. 17 Probability density of latitude error

As illustrated in Figs.16—17, the probability density values of latitude and longitude errors reveal that the KF and STKF exhibit broad distributions with low peaks and heightened instances of extreme errors. The maximum error values for all three algorithms are concentrated around zero, suggesting that the filters are capable of providing estimates that are in close proximity to the true value in the majority of instances. The MA-STKF method exhibits the highest peak, while the STKF method demonstrates the second highest peak, thereby indicating that the MA-STKF is more accurate than the STKF method. The highest peak value of the MA-STKF method in terms of latitude error is approximately zero, indicating that it has the minimal fluctuation of error and excellent stability. Moreover, it demonstrates enhanced sensitivity to the system, resilience to changes in system uncertainty, and suitability for scenarios with stringent requirements for high-precision positioning.

Figs. 18—19 give the comparison of the attitude angle errors.

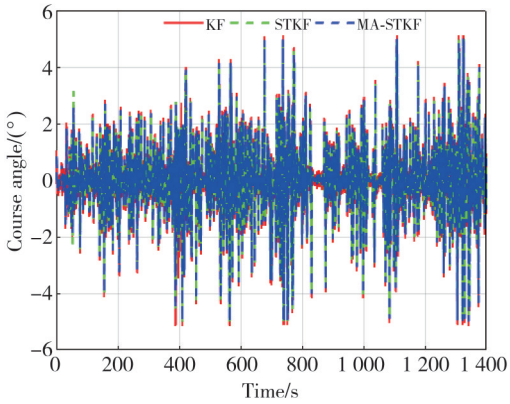

Fig. 18 Comparison of course angle errors

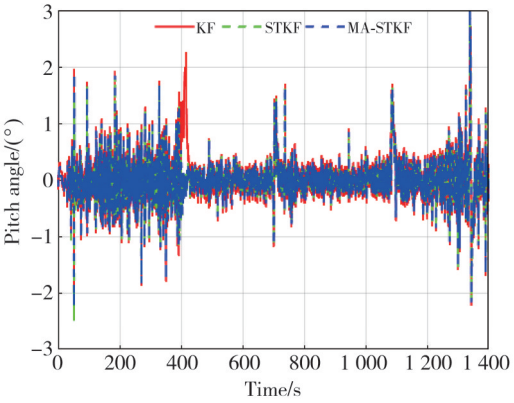

Fig. 19 Comparison of pitch angle errors

Table 5 shows the RMSEs and MADs of longitude and latitude of the three methods considered in the context of sports vehicle experiment.

Table 5 RMSEs and MADs in runway experiments

Algorithm	RMSE				MAD			
	Longitude/m	Latitude/m	Course angle/(°)	Pitch angle/(°)	Longitude/m	Latitude/m	Course angle/(°)	Pitch angle/(°)
KF	0.421 2	0.530 3	1.106 2	0.398 2	0.317 3	0.414 3	0.829 4	0.277 0
STKF	0.392 5	0.481 3	1.007 2	0.322 3	0.290 0	0.359 5	0.694 4	0.199 3
MA-STKF	**0.263 1**	**0.300 5**	**1.006 6**	**0.321 3**	**0.187 7**	**0.212 7**	**0.694 2**	**0.198 2**

As illustrated in Table 5, the RMSE and MAD of MA-STKF for both longitude and latitude are observed to be smaller than those of the KF and STKF methods. It demonstrates superior performance in terms of longitude and latitude localization, with an improvement of 37% and 33% respectively in comparison to the conventional KF, and a further enhancement of 40% and 35% respectively in contrast to the STKF method. The aforementioned evidence illustrates that the MA-STKF exhibits a high degree of filtering accuracy and is capable

of maintaining tracking of the true state even when faced with an increase in noise uncertainty.

4 Conclusions

To solve the problem of KF that the presence of external noise leads to degradation of filtering performance, an MA-STKF is proposed, which combines a measurement adaptive algorithm based on the STF with a forgetting factor designed to facilitate the online adjustment of the innovative covariance matrix, and a fault detection is carried out in order to prevent over-modification of the measurements. On-vehicle experiments show reductions in RMSEs of latitude and longitude compared to the conventional KF by 0.158 1 m and 0.229 8 m, respectively. This approach shows the potential to improve the accuracy and reliability of the system, providing valuable insights from an engineering perspective. However, the MA-STKF is unable to obtain a more accurate adaptation of the measurements due to its global estimation and processing of the system measurements. Follow-up studies could consider, for example, introducing sequential filtering for accurate estimation to ensure the long-term stability of the combined navigation effect.

Acknowledgement

This work was supported by Natural Science Foundation of Gansu Province (No.23JRRA869), Gansu Provincial Science and Technology Guidance Programme (No.2020-61-14), Gansu Province University Industry Support Programme (No. 2023CYZC-32), Major Cultivation Project of Scientific Research and Innovation Platform of Universities (No.2024CXPT-17), and National Railway Administration Project (No.KF2022-021).

Declaration of conflicting interests

The authors have no conflict of interests related to this publication.

References

[1] WEI W H, YUAN W, ZHANG Y F. Adaptive estimation method of observational model systematic errors for intelligent vehicle SINS/GNSS dynamic integrated navigation. China Journal of Highway and Transport, 2024, 37(7): 280-290.

[2] YAN Y Q, SI Y B, CHEN G W, et al. GNSS-assisted optimal alignment method for low-cost SINS motion of vehicle. Measurement Science and Technology, 2025, 36(1): 016305.

[3] LI B F, CHEN G E. Precise cooperative positioning for vehicles with GNSS and INS integration. Acta Geodaetica et Cartographica Sinica, 2022, 51(8): 1708-1716.

[4] ZHANG F, WANG K, LIAO W, et al. Lidar/MEMS IMU/Odometer integrated tightly navigation algorithm. Chinese Journal of Scientific Instrument, 2022, 43(7): 139-148.

[5] JIANG Y, PAN S, YE F, et al. Approach for detection of slowly growing fault based on robust estimation and improved AIME. Systems Engineering and Electronics, 2022, 44(9): 2894-2902.

[6] XU B, CHEN C, WANG L Z. Vehicle-mounted INS/OD/GPS integrated navigation based on IMM filtering. Journal of Chinese Inertial Technology, 2022, 30(1): 58-64.

[7] NI S, LI S, XIE Y, et al. Overview of GNSS/INS ultra-tight integrated navigation. Journal of National University of Defense Technology, 2023, 45(5): 48-59.

[8] SUN Z Q, TANG K H, WU M P, et al. High-speed train positioning method based on motion constraints suppressing INS error in tunnel. Journal of Northwestern Polytechnical University, 2021, 39(3): 624-632.

[9] WU P B, PAN S G, GAO W, et al. UWB quality control and its integrated positioning with GNSS/INS considering NLOS and system errors. Chinese Journal of Scientific Instrument, 2024, 45(5): 51-60.

[10] GUO C, CHEN Y C, LUO Y R. Matrix Lie group filtering algorithm for GNSS/SINS loosely integrated navigation in the world frame. Journal of Chinese Inertial Technology, 2024, 32(3): 242-249.

[11] YANG B, LIU F, XUE L, et al. An improved Kalman filter algorithm under colored noise. Journal of Chinese Inertial Technology, 2023, 31(10): 1004-1009.

[12] ZENG Q, ZHAO T, ZHAO B, et al. Adaptive Kalman filtering algorithm based on exponential attenuating factor for integrated navigation system. Journal of Chinese Inertial Technology, 2021, 29(3): 307-313.

[13] JIN K D, CHAI H Z, SU C H, et al. Fading memory variational Bayesian adaptive filter based on variable attenuating factor. Journal of Beijing University of Aeronautics and Astronautics, 2023, 49(11): 2989-2999.

[14] ZHAO B, ZENG Q H, LIU J Y, et al. Fault detection and robust adaptive filter algorithm based on smooth bounded layer. Journal of Chinese Inertial Technology, 2023, 31(3): 245-253.

[15] HU X, PAN X, LIU C. An Improved Sage-Husa adaptive filtering algorithm for GNSS/SINS integrated navigation . Journal of Geodesy and Geophysics, 2023, 43(8): 791-794.

[16] XIONG X, HUANG G, WANG X. Adaptive robust cubature Kalman filter integrated navigation algorithm based on Chi-Square Test. Journal of Detection &. Control, 2019, 41(5): 125-131.

[17] ZHOU D, XI Y, ZHANG Z. Extended Kalman filtering with suboptimal fading factor for nonlinear systems. Control and Decision, 1990(5): 1-6.

[18] HU H, YAN Y J, OU M H, et al. Application of adaptive strong tracking Kalman filter based on fuzzy logic to GPS

positioning. GNSS World of China, 2017, 42(1): 6-11.
[19] LÜ D H, WANG J Q, XIONG K, et al. Strong tracking Kalman filter for non-Gaussian observation. Control Theory & Applications, 2019, 36(12): 1997-2004.
[20] LI S X, HUANG F R, QIU S Q, et al. SINS/Odometer integrated navigation method based on adaptive strong tracking filter. Journal of Chinese Inertial Technology, 2018, 26(2): 156-161.
[21] XIONG X, HUANG G Y, WANG X D. Strong tracking SVDCKF integrated navigation algorithm based on multiple fading factors. Journal of Chongqing University of Posts and Telecommunications (Natural Science Edition), 2021, 33(2): 330-336.
[22] XUE W T, ZHANG B, LI S J. Application of new information adaptive Kalman filter in integrated navigation. GNSS World of China, 2014, 39(4): 8-11.
[23] YAN G, WENG J. Strapdown inertial navigation algorithm and integrated navigation principle. Xi'an: Northwestern Polytechnical University Press, 2019(1): 121-127.
[24] XIA Q J, SUN Y X, ZHOU C H. An optimal adaptive algorithm for fading Kalman filter and its application. Acta Automatica Sinica, 1990, 16(3): 210-216.
[25] JING L, LIN X Y, PAN X L, et al. Research on GNSS/SINS integrated navigation adaptive UKF algorithm based on improved Sage-Husa. Chinese Space Science and Technology, 2024, 44(5): 127-135.

基于SINS/GNSS/ODO组合导航的改进强跟踪卡尔曼滤波算法

春　意[1,2]，陈光武[2,3*]，司涌波[2,3]，周　鑫[2,3]，严玉乾[2,3]

1. 兰州交通大学 电子与信息工程学院，甘肃 兰州 730070；
2. 甘肃省高原交通信息通信工程及控制重点实验室，甘肃 兰州 730070；
3. 兰州交通大学 自动化与电气工程学院，甘肃 兰州 730070

摘　要：捷联式惯性导航系统（Strapdown inertial navigation system，SINS）、全球导航卫星系统（Global navigation satellite system，GNSS）和里程表（Odometer，ODO）的结合是目前实现车辆多源融合导航系统最实用、最经济的方法。然而，传统的卡尔曼滤波算法会受到车辆运行过程中系统状态矩阵和测量噪声协方差矩阵不准确的影响，导致导航定位精度下降。为解决这一问题，提出了一种测量自适应跟踪滤波方法（Measurement adaptive strong tracking Kalman filter，MA-STKF）。该算法采用渐消加权的方式，考虑实际滤波的新息时间序列估计量测协方差阵，引入量测遗忘因子，进行实时估计和校正，并与强跟踪滤波器的衰落因子相结合，利用实际测量误差与预测协方差的差异，重新设定衰落因子，提高了算法的跟踪性能。将提出的算法应用于SINS/GNSS/ODO组合导航系统进行仿真实验和跑车实验，结果表明，该算法相对于卡尔曼滤波（Kalman filtering，KF）和强跟踪滤波（Strong tracking Kalman filter，STKF），其定位经度分别提升约52.48%和30.96%，定位纬度分别提升约63.27%和37.64%。

关键词：卡尔曼滤波；组合导航；强跟踪滤波；量测自适应；遗忘因子

引用格式：CHUN Yi, CHEN Guangwu, SI Yongbo, et al. Improved strong tracking Kalman filter algorithm based SINS/GNSS/ODO integrated navigation. Journal of Measurement Science and Instrumentation, 2026, 17(1): 61-71. DOI: 10.62756/jmsi.1674-8042.2026005